HiSST: 2nd International Conference on
High-Speed Vehicle Science & Technology
11–15 September 2022, Bruges, Belgium

Direct molecular simulation of dissociating oxygen-nitrogen mixture in space-homogeneous reactor

Erik Torres[1], *Thomas E. Schwartzentruber*[1]

Abstract

In this paper we present first-principles direct molecular simulations (DMS) of rovibrational excitation and dissociation of five-species air (N_2, O_2, NO, N, O) mixtures in constant-volume reactors under isothermal and adiabatic conditions. Our simulations are restricted to a static gas in space-homogeneous reservoirs without flow coupling, but we carefully choose initial conditions to mimic the nonequilibrium state encountered behind strong shock fronts, such as the ones generated in shock-tube facilities, or ahead of hypersonic flight vehicles. We examine non-Boltzmann effects in the rotational and vibrational energy distributions of the O_2-, N_2 and NO-molecules, as well as the temperatures associated with their rotational and vibrational modes during the quasi-steady-state dissociation regime. By examining probability density distributions of the diatomic species consumed in the dissociation and the Zel'dovich exchange reactions, we are able to assess their degree of rovibrational biasing. It is found that all dissociating diatoms exhibit a strong preference toward internal energies near the dissociation limit, whereas the same does not happen in the exchange reactions.

Keywords: *thermo-chemical nonequilibrium, molecular dissociation, Zel'dovich reactions, ab initio potential energy surfaces, direct molecular simulation*

1. Introduction

The Direct Molecular Simulation (DMS) method is a variant of direct simulation Monte Carlo [1] (DSMC) wherein collision outcomes are determined directly via classical trajectory calculations on potential energy surfaces (PES), instead of the semi-empirical chemistry models commonplace in DSMC. Since it relies entirely on potentials to determine collision outcomes, DMS is capable of naturally predicting the rovibrationally coupled internal energy excitation and dissociation of the gas under nonequilibrium conditions with high accuracy and without any experimentally tuned model parameters. Thus, in conjunction with quasi-classical trajectory (QCT) studies [2, 3], it can be used as a reference tool for the development of reduced-order nonequilibrium chemical-kinetics models for DSMC, or computational fluid dynamics (CFD).

The origins of DMS can be traced back to the Classical Trajectory DSMC (CT-DSMC) method proposed by Koura [4, 5]. Starting with a CT-DSMC implementation by Norman et al. [6], it has been under continued development in our group for the last decade. For an overview of the method's basics and early development, refer to Schwartzentruber et al. [7] and references cited therein. The most recent work has focused on taking advantage of the growing set of multi-body *ab initio* potentials generated by the computational chemistry group at the University of Minnesota. Valentini et al. [8, 9] focused on direct molecular simulations of nitrogen dissociation and relied on the $N_2 - N_2$ PES by Paukku et al. [10]. Grover et al. [11, 12] used DMS to study coupled rovibrational excitation and dissociation of oxygen in space-homogeneous heat baths with the help of three ground-electronic-state $O_2 - O_2$ potentials by Paukku et al. [13, 14] and nine additional $O - O_2$ potentials by Varga et al. [15]. Since then, DMS has been extended to increasingly more complex problems. Torres et al. [16, 17] used DMS to simulate nitrogen and oxygen dissociation in adiabatic reservoirs representative of post-shock conditions. From

[1] *Department of Aerospace Engineering and Mechanics, University of Minnesota, 107 Akerman Hall, 110 Union St SE, Minneapolis, MN, 55455, etorres@umn.edu, schwart@umn.edu*

there on, the method has been applied to the study of nonequilibrium chemistry across normal shocks in oxygen [18], as well as nitrogen dissociation around cylinders in hypersonic cross-flow [19, 20].

Our most recent work has focused on integrating the Minnesota *ab initio* potentials for mixed nitrogen, oxygen and nitric oxide interactions in order to perform first-principles studies of the fully coupled nonequilibrium chemistry of a five-species air mixture (N_2, O_2, NO, N, O) in the ground electronic state. For N_2 – O_2 and NO – NO interactions we now rely on the triplet PES by Varga et al. [21]. Trajectory calculations for species pairs O_2 – N and NO – O are carried out on the three ground state potentials by Varga et al. [21], while those for pairs N_2 – O and NO – N rely on two additional potentials by Lin et al. [22]. The most up-to-date discussion of our 5-species air DMS implementation can be found in Ref. [23]. This reference also contains recent characteristic rotational and vibrational relaxation times for air species determined via DMS calculations. These first-principles results, along with new QCT-derived rate coefficients for the Zel'dovich exchange reactions are being used to update and enhance chemical kinetic models for CFD [24].

2. Direct Molecular simulations of coupled rovibrational relaxation and nonequilibrium chemistry of 5-species air mixture

2.1. Isothermal reactor

We begin by studying the nonequilibrium chemistry in a 5-species air mixture (comprising N_2, O_2, NO, N and O all in their respective ground electronic states) in a space-homogeneous, constant-volume reservoir under isothermal (constant translational temperature T) conditions. In recent work [23] we reported on the first such direct molecular simulation, where the heat bath translational temperature was kept at $T = 10\,000$ K. A total of $100\,000$ DMS particles were used to represent the initial mixture, which was comprised of molecular nitrogen and oxygen at a molar ratio of 80/20. The initial number density in the reactor was set to $n_0 = 10^{24}$ m^{-3}. The internal (rotational and vibrational) energies of all particles belonging to both molecular species were initialized to conform to Boltzmann distributions at $T_{\text{vib}} = T_{\text{rot}} = 300$ K, whereas their initial center-of mass velocities were randomly sampled from Maxwellian distributions at $T = 10\,000$ K. This large initial temperature difference between the translational and internal energy modes was meant to mimic the conditions behind a strong shock wave, where the compression of the cold, free-stream gas across the shock happens so suddenly that it raises the translational temperature almost instantly, while the internal degrees of freedom and the chemical composition initially remain "frozen" at their free-stream values. It is only during the subsequent internal energy relaxation and chemical transformation phase that the gas mixture begins to adjust to the new conditions. Here we re-examine the test case from Ref. [23] to gain further insight into the microscopic behavior of the gas during this phase.

The internal energy relaxation process is shown in Fig. 1, where we plot temperature profiles for the rotational (upper plot), vibrational (middle plot) and combined internal (lower plot) modes of the diatomic species. Since the overall internal energy of the gas is divided among the three diatomic species, separate rotational, vibrational and internal mode temperatures for each diatom (N_2 in red, O_2 in blue and NO in green) are reported. The three diatomic species each relax at their own rate, which is why each temperature profile follows its own distinct trajectory. In particular, the behavior observed for nitric oxide differs considerably from that of the other two diatomic species. Whereas the rotational and vibrational temperatures of N_2 and O_2 rise over time from their initially imposed values around 300 K, gradually approaching the imposed heat bath translational temperature of $10\,000$ K, no nitric oxide molecules are initially present in the mixture. Thus, the internal mode temperatures of NO are initially undefined. Only after chemical reactions in the gas produce the first few nitric oxide molecules do its internal mode temperatures begin to take on finite values. As it turns out, these molecules are formed "internally hot", reflected by rotational and vibrational temperatures (green lines in Fig. 1) well above those of the other two diatomic species, as well as above the reservoir translational temperature. Early on, the internal mode temperatures of NO exhibit large fluctuations and are subject to large statistical uncertainties. This is because they must be determined from the very small sample size of DMS particles initially representing NO molecules. However, as time progresses, more and more such molecules are

produced and subsequently become involved in inelastic collisions with the other mixture components. This results in the gradual "evening out" of the NO temperature profiles and relaxation of its internal energy modes toward the heat bath temperature.

The internal mode temperatures of N_2 and O_2 exhibit a different behavior. Focusing on the rotational mode first (top of Fig. 1), one sees that both molecular nitrogen and oxygen (red and blue lines respectively) relax at almost the same rate and their respective rotational temperatures very quickly approach the heat bath temperature. Bigger discrepancies are observed between the vibrational temperature profiles (middle plot of Fig. 1) for both species. Molecular oxygen relaxes toward the heat bath temperature more quickly than nitrogen. As the O_2 vibrational temperature approaches the heat bath temperature, it levels off and begins to oscillate around a near-constant value a few hundred kelvin below $T = 10\,000\,\mathrm{K}$. Molecular nitrogen takes about five times as long to vibrationally relax. A vertical dashed line (at $t = 1\,\mu\mathrm{s}$) in all sub-plots of Fig. 1 marks the estimated end of the internal energy excitation phase. Beyond this time, the vibrational temperatures of all three diatomic species remain nearly constant, except for statistical fluctuations around their mean values. Crucially, during this phase the vibrational temperatures do not fully equilibrate with the heat bath temperature. The offset from $T = 10\,000\,\mathrm{K}$ is most pronounced for O_2, less so for NO and almost zero for N_2. In this intermediate state, the mixture has not yet reached full thermal, nor chemical equilibrium and dissociation reactions involving the three diatomic species preferentially split molecules with internal energies close to their respective dissociation limits $D_0^{N_2}$, $D_0^{O_2}$ and D_0^{NO} into atomic nitrogen and oxygen. At the same time, inelastic collisions continue to rovibrationally excite molecules from lower-lying energy levels, helping to partially replenish the high-energy populations of diatoms being lost to dissociation. The time window during which this dynamic balance between depletion and replenishment prevents the internal energy populations of the diatomic species from reaching their equilibrium Maxwell-Boltzmann distributions at the reservoir temperature is termed the quasi-steady-state (QSS) dissociation phase and, as can be seen in Fig. 1, lasts for the remainder of the simulated time.

Figure 2 shows mole fraction profiles for all five species corresponding to the same time window of Fig. 1. Starting from a mixture containing only molecular nitrogen and oxygen (solid red and blue lines), dissociation reactions gradually cause atomic nitrogen and oxygen (dashed red and blue lines) to appear. These atomic species subsequently react with the remaining molecular nitrogen and oxygen to produce nitric oxide (solid green line) in the Zel'dovich exchange reactions $N_2 + O \rightleftharpoons NO + N$ and $O_2 + N \rightleftharpoons NO + O$. As more and more NO is produced this way, its mole fraction continues to increase until reaching a peak of $x_{NO} \approx 0.17$ roughly $0.7\,\mu\mathrm{s}$ from the beginning of the simulation. Nitric oxide then increasingly reacts with the other species in the mixture in the reverse sense of the Zel'dovich reactions. This partially replenishes the amounts of molecular nitrogen and oxygen and removes some NO from the mixture. Simultaneously, all three diatomic species continue to dissociate into their atomic constituents. Since our direct molecular simulations currently do not account for recombination reactions, there is no mechanism present that would balance out these dissociation reactions in the long term. Therefore, over long enough times our simulations predict that the mole fractions of all three diatomic species should theoretically approach zero, with only atomic nitrogen and oxygen remaining.

There are many more chemical reactions occurring in parallel to the few just mentioned. A complete list of all the ones being accounted for in our DMS calculations was presented in Table 2 of Ref [23]. We refer to Sections II.C and II.D of that paper for a more in-depth discussion on how QSS rate coefficients for these reactions were extracted from our DMS calculations. Here, we will focus instead on a few new results that complement Ref. [23]. In particular, we examine the internal energy population distributions adopted by the three diatomic species during the QSS phase. First, in Fig. 3(a) we plot the internal (i.e. combined rotational and vibrational) energy distribution for molecular nitrogen. Continuing with the practice from previous work [25, 18], we have sub-divided the internal energy scale of N_2 into a set of contiguous energy bins, each one encompassing a small energy interval. This scale spans from zero to the maximum possible rovibrational energy for N_2 molecules ($E_{max}^{N_2} = 15.12\,\mathrm{eV}$) in the ground electronic state. A vertical dashed line in Fig. 3(a) marks the dissociation energy for molecular nitrogen at $D_0^{N_2} = 9.75\,\mathrm{eV}$. This line serves to separate all molecules populating *bound* energy levels below $D_0^{N_2}$ from those populating *quasi-bound* levels above it. All N_2-populations extracted from DMS end up being

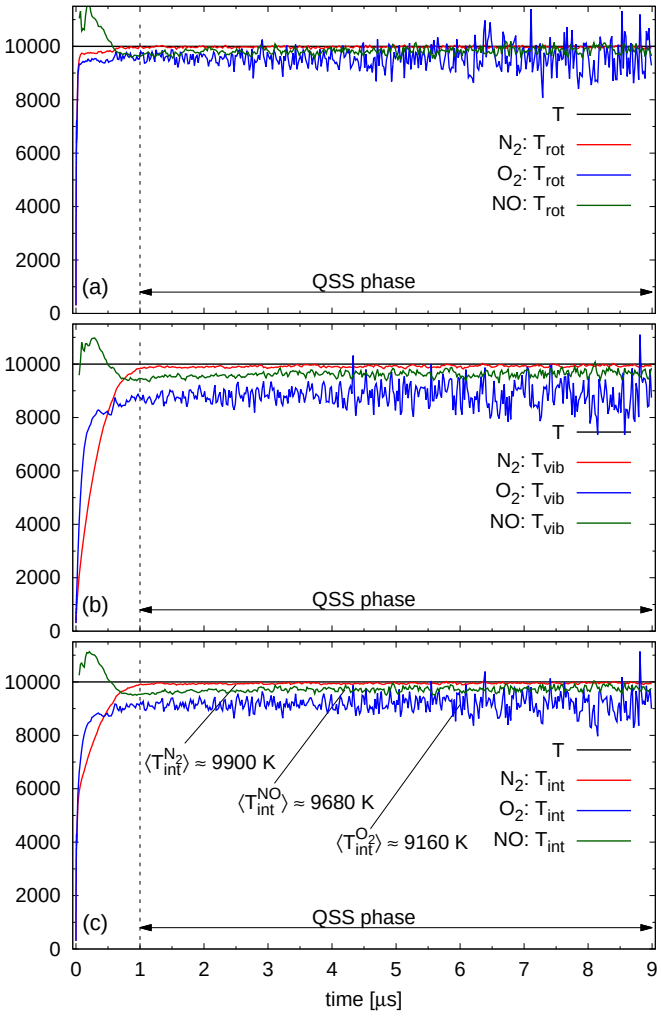

Fig 1. DMS of isothermal reactor at $T = 10\,000$ K: rotational (upper plot), vibrational (middle plot) and internal (bottom plot) temperature profiles [K] for N_2 (red), O_2 (blue) and NO (green).

grouped into one of 80 equally-spaced bins in the bound, or 42 bins in the quasi-bound energy range. Thus, the distribution plotted using red squares in Fig. 3(a) represents the time-average populations over the entire duration of the simulated QSS phase (recall Fig. 1) normalized by the total number of N_2-molecules sampled during that time frame:

$$f(\bar{E}_{\mathrm{N_2}(k)}) = \frac{N_{\mathrm{N_2}(k)}}{\sum\limits_{k \in \mathcal{K}_{\mathrm{N_2}}} N_{\mathrm{N_2}(k)}} \tag{1}$$

For comparison, the curve in black in Fig. 3(a) represents the Boltzmann distribution at $T_{\mathrm{int}} = 9\,900$ K, which is the approximate time-averaged internal temperature of N_2 during the QSS interval (see Fig. 1(c)). Both these distributions represent a sample of molecular nitrogen at the same average internal energy, only that the QSS distribution exhibits a depleted high-energy tail near and above $D_0^{\mathrm{N_2}}$, whereas the Boltzmann distribution does not. The depletion of the distribution's tail can be attributed to the aforementioned preferential dissociation from this range of internal energies. During the QSS phase, dissociation rates from these high-energy levels are so high that excitation reactions cannot fully compensate for

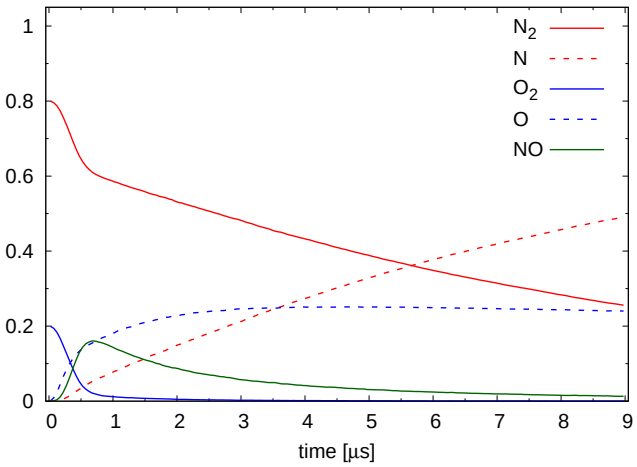

Fig 2. DMS of isothermal reactor at $T = 10\,000$ K: mole fractions of air-5 species: N_2 solid red, N dashed red, O_2 solid blue, O dashed blue, NO solid green line.

the molecules lost. This prevents the high-energy populations to fully attain the Boltzmann distribution shown. The macroscopic effect is that the dissociation rates during QSS are effectively constrained by the replenishment rates due to rovibrational excitation. In this, and in previous work we have observed that, depending on the reaction in question, the QSS dissociation rates tend to be 2-4 times lower than the corresponding equilibrium rates at the same internal temperature.

The time-averaged QSS distributions for molecular oxygen and nitric oxide present a qualitatively similar behavior. However, due to their molecular structures, the populated internal energy ranges ($E_{\text{max}}^{\text{O}_2} = 8.386$ eV and $E_{\text{max}}^{\text{NO}} = 10.10$ eV) and dissociation energies are different ($D_0^{\text{O}_2} = 5.11$ eV and $D_0^{\text{NO}} = 6.49$ eV) and so are the number of bound and quasi-bound internal energy bins (42+26 for O_2 and 53+29 for NO) used to group the rovibrational energy levels. In Fig. 3(b), we see that the time-averaged internal energy distribution of O_2 during QSS (blue symbols) possesses a depleted tail relative to the Boltzmann distribution at $T_{\text{int}} = 9160$ K, much in the same way as was seen for nitrogen. Again, is it mostly energy levels near and above the dissociation limit which are affected. The picture is similar for nitric oxide. Its QSS distribution is shown as green symbols in Fig. 3(c) together with the corresponding Boltzmann distribution evaluated at NO's average internal temperature $T_{\text{int}} = 9680$ K during the QSS phase.

Apart from internal energy distributions of the three diatomic species themselves, DMS can be used to collect information on the internal energy probability density functions (pdfs) for each diatomic species being consumed in specific chemical reactions. In past work [26, 25], such reaction probability density functions have been gathered from DMS calculations for "pure" nitrogen dissociation (i.e. $N_2 + N_2 \longrightarrow 2\,N + N_2$ and $N_2 + N \longrightarrow 3\,N$), but also for oxygen dissociation [17] (i.e. $O_2 + ON \longrightarrow 2\,O + O_2$ and $O_2 + O \longrightarrow 3\,O$). In this work, we now apply the same sampling procedures to a number of additional relevant reactions taking place in a five-species air mixture. In particular, we focus on the atom-diatom reactions involving "mixed" collision pairs, such as N_2 + O, O_2 + N, etc. The reactions in question are summarized in Table 1. As can be seen, for each reactant species pair, there are essentially two outcomes of interest (1) *dissociation* of the diatomic species into its constituents, or (2) *exchange* of one atomic nucleus from the original diatom leading to new product diatomic and atomic species.

In Fig. 4 we examine two pdfs for the reactions involving collision partners N_2 + O in the upper half and NO + N in the other lower half. Focusing on Fig. 4(a) first, we define the dissociation pdf for the reaction $N_2 + O \rightarrow 2\,N + O$ as:

$$p_{\text{N}_2+\text{O}}^{\text{diss}}(\bar{E}_{\text{N}_2(k)}) = \frac{N_{[\text{N}_2(k)+\text{O}\rightarrow 2\,\text{N}+\text{O}]}}{\sum\limits_{k\in\mathcal{K}_{\text{N}_2}} \{N_{[\text{N}_2(k)+\text{O}\rightarrow 2\,\text{N}+\text{O}]}\}}, \tag{2}$$

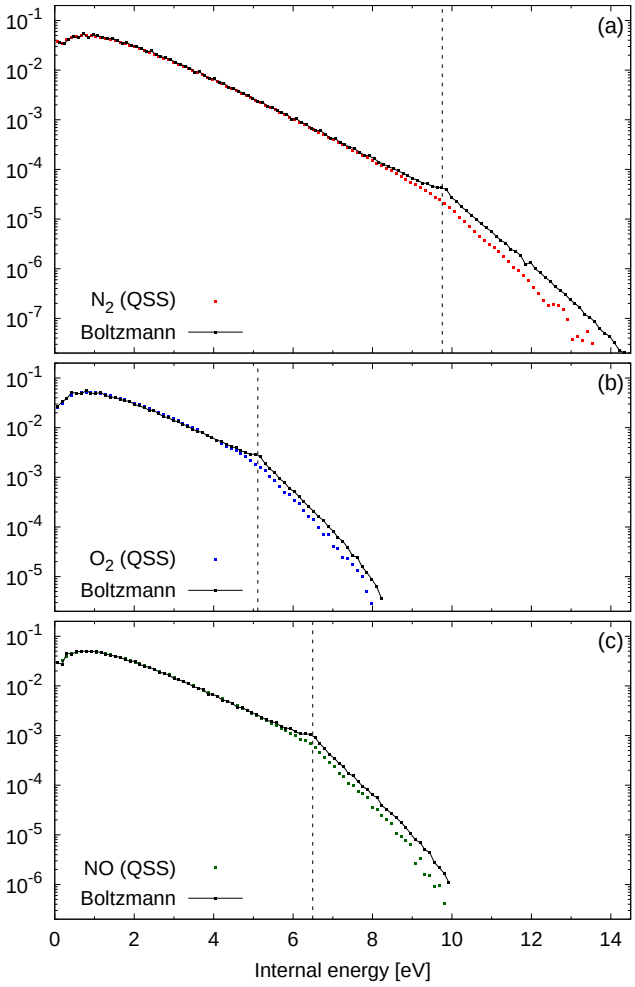

Fig 3. DMS of isothermal reactor at $T = 10\,000$ K: Normalized population distributions of diatomic species during QSS phase. Boltzmann distributions for each diatom at $\langle T_{\text{int}} \rangle$ during QSS.

where $N_{[\text{N}_2(k)+\text{O}\rightarrow 2\,\text{N}+\text{O}]}$ in the numerator represents the number of dissociation events for N_2 molecules with internal energies belonging to bin $\bar{E}_k$, which were recorded over the QSS sampling period. The sum over all energy intervals $k \in \mathcal{K}_{\text{N}_2}$ in the denominator then represents the overall number of N_2 + O dissociation events over the sampling period. This pdf is plotted in Fig. 4(a) using red squares. Despite some statistical noise, it can be seen that it spreads over the entire internal energy range of N_2, but exhibits a strong peak around 9.75 eV, precisely at the dissociation energy of molecular nitrogen. The dissociation pdf quickly drops off from there in both directions. The least likely N_2 molecules to dissociate in this reaction are both those with the lowest and the highest internal energies. This behavior is fully consistent with what has been observed in the aforementioned Refs. [26] and [25] for N_2 dissociation induced by collision with other N_2-molecules, or N-atoms. For comparison, the curve plotted using gray symbols represents the internal energy distribution of N_2 during QSS and is a re-plot from Fig. 3(a). When comparing the dissociation pdf (red symbols) with the internal energy distribution (gray symbols), it becomes clear that the diatoms undergoing dissociation do not closely conform to the latter, but are preferentially selected from the narrow energy range around $D_0^{\text{N}_2}$.

In analogy to Eq. (2) we define an equivalent exchange pdf for the first Zel'dovich reaction $N_2 + O \rightarrow$

Table 1. Reactions selected for sampling reaction pdfs in Figs. 4 and 5

reactants	type	products
N_2 + O $\longrightarrow$	diss.	2 N + O
	exch.	NO + N
NO + N $\longrightarrow$	diss.	2 N + O
	exch.	N_2 + O
O_2 + N $\longrightarrow$	diss.	2 O + N
	exch.	NO + O
NO + O $\longrightarrow$	diss.	2 O + N
	exch.	O_2 + N

NO + N:

$$p^{\text{exch}}_{\text{N}_2(k)+\text{O}}(\bar{E}_{\text{N}_2(k)}) = \frac{\sum\limits_{l\in\mathcal{K}_{\text{NO}}}\{N_{[\text{N}_2(k)+\text{O}\rightarrow\text{NO}(l)+\text{N}]}\}}{\sum\limits_{\substack{k\in\mathcal{K}_{\text{N}_2}\\ l\in\mathcal{K}_{\text{NO}}}}\{N_{[\text{N}_2(k)+\text{O}\rightarrow\text{NO}(l)+\text{N}]}\}}, \tag{3}$$

which represents the ratio of internal energy-specific exchange events relative to the total number of exchange reaction events during the QSS phase. Note that the numerator (but also the denominator) includes a sum over all internal energies of NO, since we are only interested in the dependence on the pre-collision energies of nitrogen: $\bar{E}_{\text{N}_2(k)}$. The result of Eq. (3) is plotted in Fig. 4(a) using blue symbols. As can be seen, this exchange pdf differs considerably from the dissociation pdf shown in red. First, the exchange pdf does not exhibit the same peak around $D_0^{\text{N}_2}$. Instead, the maximum of the exchange pdf is shallower and appears at much lower internal energies (roughly around the $3\,$eV mark). Indeed, the shape of the exchange pdf, though not in perfect agreement, shows a much closer resemblance to the QSS internal energy distribution of N_2 (in gray). Thus, the exchange reaction is seen to exhibit much weaker selectivity towards specific reactant internal energies than dissociation.

Going down the list of Table 1, next we examine the dissociation and exchange pdfs for the reactant pair NO + N. Analogous to Eqs. (2) and (3), their definitions are:

$$p^{\text{diss}}_{\text{NO}+\text{N}}(\bar{E}_{\text{NO}(k)}) = \frac{N_{[\text{NO}(k)+\text{N}\rightarrow 2\,\text{N}+\text{O}]}}{\sum\limits_{k\in\mathcal{K}_{\text{NO}}}\{N_{[\text{NO}(k)+\text{N}\rightarrow 2\,\text{N}+\text{O}]}\}}, \tag{4}$$

for the NO + N dissociation pdf and

$$p^{\text{exch}}_{\text{NO}(k)+\text{N}}(\bar{E}_{\text{NO}(k)}) = \frac{\sum\limits_{l\in\mathcal{K}_{\text{N}_2}}\{N_{[\text{NO}(k)+\text{N}\rightarrow\text{N}_2(l)+\text{O}]}\}}{\sum\limits_{\substack{k\in\mathcal{K}_{\text{NO}}\\ l\in\mathcal{K}_{\text{N}_2}}}\{N_{[\text{NO}(k)+\text{N}\rightarrow\text{N}_2(l)+\text{O}]}\}}, \tag{5}$$

for the NO + N exchange pdf respectively. In Fig. 4(b), we plot the result of Eq. (4) in red and that of Eq. (5) using blue symbols. The gray symbols represent the time-average internal energy distribution of NO during the QSS phase (green symbols carried over from Fig. 3(c)). The results follow a similar pattern to those for N_2 + O. However, since the dissociation energy for nitric oxide lies at $D_0^{\text{NO}} = 6.49,$ eV, the characteristic peak of the dissociation pdf is centered around that value instead. The exchange pdf for NO + N is even closer to the internal energy distribution of NO than was the case for N_2. This implies almost no bias of the reverse exchange reaction towards specific internal energies of the reactant NO molecules.

We carry out the same analysis for the remaining reactions in Table 1. The dissociation and exchange pdfs for the O_2 + N pair are plotted in Fig. 5(a) as the red and blue symbols respectively, together

with the internal energy distribution of O_2 during the QSS phase in gray. The dissociation pdf of O_2 + N exhibits a peak at the dissociation energy $D_0^{O_2} = 5.11\,\text{eV}$ and drops off quickly towards lower- and higher-energy intervals. The exchange pdf of O_2 + N by contrast closely conforms to the shape of the QSS internal energy distribution of O_2, confirming the lack of preferential reactivity for this process. Finally, the dissociation and exchange pdfs for the NO + O pair are plotted in Fig. 5(b) as the red and blue symbols respectively, together with the internal energy distribution of NO during the QSS phase in gray. The dissociation pdf of NO + O exhibits the now expected peak at $D_0^{NO} = 6.49\,\text{eV}$ and drops off quickly towards lower- and higher-energy levels. The exchange pdf possesses a shape that resembles the one of N_2 + O, albeit only spanning the internal energy range of NO. As for all preceding reactant pairs, the exchange reaction does not exhibit as strong a bias towards specific reactant internal energies as the dissociation does.

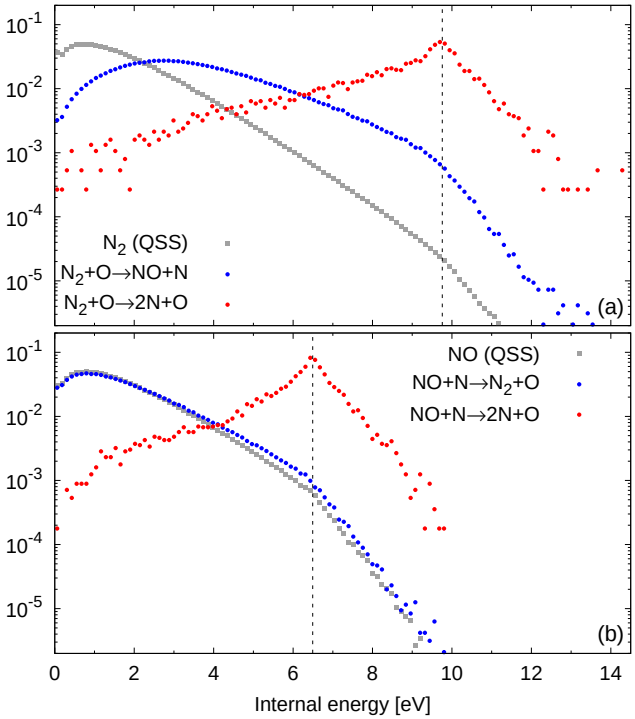

Fig 4. DMS of isothermal reactor at $T = 10\,000\,\text{K}$: Reaction probability density functions for reactant pairs N_2 + O and NO + N during QSS phase

2.2. Adiabatic reactor

The test case of Sec. 2.1 simulated an isothermal reactor in which the heat bath translational temperature T was artificially kept constant over time. In this section we carry out a similar calculation, only that we replace the isothermal reactor with an adiabatic one. In this scenario the total energy of the gas mixture remains constant, while T changes along with the internal mode temperatures in response to internal energy relaxation and chemical processes taking place in the reactor. Since T is no longer fixed under adiabatic conditions, its value at the beginning of the simulation must be specified as part of the initial conditions. Together with the initial internal mode temperatures, density and imposed mixture composition, it fixes the total energy of the system. As was the case in Sec. 2.1, we are interested in approximately reproducing the thermo-chemical nonequilibrium conditions created behind a strong shock front. Even though it is possible nowadays to simulate a full normal shock wave with DMS [18], obtaining such solutions is computationally costly and beyond the scope of this paper.

Instead, we resort to the procedure we first outlined in Ref. [16] to come up with representative initial conditions for the adiabatic reactor. We first specify the free-stream conditions upstream of the normal

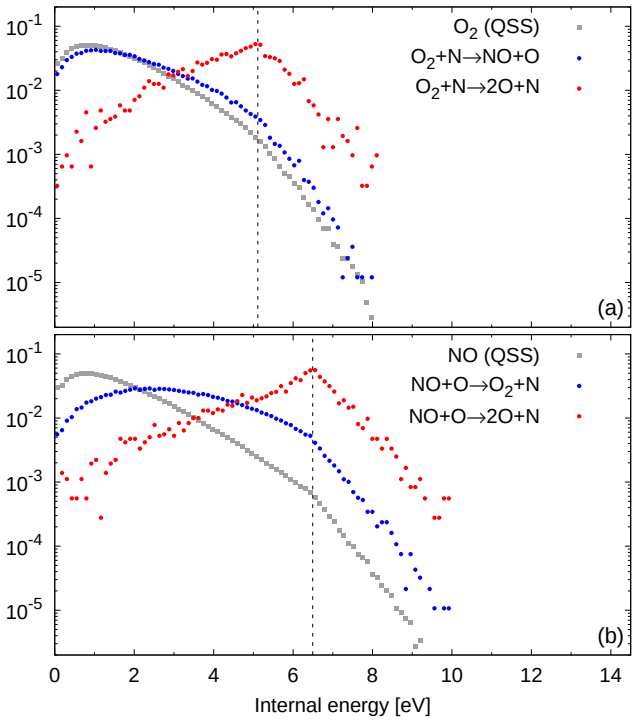

Fig 5. DMS of isothermal reactor at $T = 10\,000$ K: Reaction probability density functions for reactant pairs O_2 + N and NO + O during QSS phase

shock we wish to approximate. The chosen conditions are summarized in the *upstream* column of Table 2. Here we have chosen a free-stream speed $u_1 = 6$ km/s and a gas temperature and composition roughly equivalent to ambient air. The rather low upstream pressure of $p_1 = 15$ Pa was arbitrarily chosen to approximate those encountered during high-altitude hypersonic flight. As can be seen, the total enthalpy of the flow $h_0 = 18$ MJ/kg upstream of the shock is effectively all due to the high flow kinetic energy $\frac{1}{2}|u_1|^2$. Based on these upstream conditions, we compute the corresponding post-shock equilibrium conditions by applying the Rankine-Hugoniot jump relations for a chemically reacting gas. The thermodynamic properties (species specific heats, enthalpies and equilibrium constants) used in this calculation account for the partial excitation of the diatomic species' vibrational degrees of freedom, but explicitly exclude effects of electronic excitation. This restriction makes the predicted post-shock equilibrium state more consistent with our DMS calculations, which can at present only account for diatomic and atomic species in their ground electronic states. Based on our estimates (see Sec.2 of Ref. [24]), neglecting the contribution of electronic energy only introduces a significant error for Air5-mixtures at temperatures well in excess of $\approx 5\,000$ K and thus is not of major concern for the case studied here. The resulting post-shock conditions are listed in the *downstream* column of Table 2.

The next step is to back out the initial translational temperature T_0 for the adiabatic reactor, which leads to the same equilibrium thermodynamic state as in the post-shock gas from Table 2. Since the adiabatic reactor by construction simulates a gas at constant (typically zero) velocity, any contribution of the post-shock flow kinetic energy $\frac{1}{2}|u_2|^2$ to the total enthalpy is inaccessible during such a 0D-reactor simulation. Instead, we assume that the gas in the "equivalent" adiabatic reactor remains at zero bulk velocity and set the enthalpy of the reactor to the same as the post-shock static enthalpy $h_2 = 17.92$ MJ/kg. This ensures that, at its final equilibrium, the gas in the reactor will reach the same mixture composition, temperature and pressure as behind the normal shock. We assume that the gas in the adiabatic reactor is initially rovibrationally and chemically frozen at the upstream state from Table 2. Thus, we *impose* as initial mixture composition and initial internal mode temperature $T_{\text{int},0} = T_{\text{rot},0} = T_{\text{vib},0}$ the ones from

Table 2. normal shock relations

Case 6k:		(1) upstream	(2) downstream
u	[m/s]	6000	410.5
p	[Pa]	15.00	5825
T	[K]	300.0	5608
x_{N_2}		0.80000	0.4050
x_{O_2}		0.20000	0.0000
x_{NO}		0.00000	0.0019
x_{N}		0.00000	0.3136
x_{O}		0.00000	0.2794
ρ	[kg/m^3]	1.733×10^{-04}	2.532×10^{-03}
h	[MJ/kg]	0.00	17.92
$\frac{1}{2}u^2$	[MJ/kg]	18.00	0.08
h_0	[MJ/kg]	18.00	

the upstream column of Table 2. This leaves T_0 as the only missing parameter. These resulting initial conditions for the adiabatic reactor are listed in column *initial NEQ* of Table 3.

Table 3. 6 km/s "equivalent" adiabatic reactor

Case 6k:		initial NEQ	final EQ
p	[Pa]	26 730	5 825
T_t	[K]	36 570	5 608
T_{int}	[K]	300	5 608
x_{N_2}		0.8000	0.4050
x_{O_2}		0.2000	0.0000
x_{NO}		0.0000	0.0019
x_{N}		0.0000	0.3136
x_{O}		0.0000	0.2794
ρ	[kg/m^3]	2.532×10^{-03}	
h	[MJ/kg]	17.92	

As was the case for the isothermal reactor, we use $80\,000$+$20\,000$ DMS particles to represent the initial N_2+O_2-mixture. Given the much lower gas density in this adiabatic reactor, the mean collision time increases from the case studied in Sec. 2.1. This has the knock-on effect of increasing the time scales over which rovibrational and chemical relaxation take place. However, some general trends are recovered in both types of scenarios. First, in Fig. 6 we plot the evolution of the translational and internal mode temperatures over the first 35 microseconds from the initial nonequilibrium state. Following the same conventions introduced for Fig. 1, the upper, middle and lower sub-plots show rotational, vibrational and combined internal temperatures for all three diatomic species respectively. The mixture translational temperature T is shown as the continuous black line in all three sub-plots. As can be seen, T drops quickly from its initial value above $36\,000$ K to somewhere around $11\,000$ K in the first 5 microseconds. From there on, it continues to decrease, but at a much slower rate.

As seen in Fig. 6(a), the rotational temperatures of molecular nitrogen and oxygen rise the quickest and reach peak values of roughly $16\,500$ K and $14\,000$ K respectively in the first few microseconds. Past this point, both N_2 and O_2 relax at slightly different rates toward the simultaneously decreasing translational temperature. As was the case for isothermal reactor, as soon as the first nitric oxide molecules are

formed, their rotational temperature starts out at a value above the other two diatomic species and closer to the translational temperature. With regard to the vibrational temperature, N_2 takes about five times longer to equilibrate with the translational mode than rotation. Initially, O_2 excites vibrationally at the same rate as N_2. However, past the first 1-2 microseconds, the vibrational temperature of O_2 quickly levels off and remains 1000-2000 kelvin below the translational temperature. Indeed, for the remainder of the simulated time it never surpasses the $10\,000$K-threshold. The vibrational temperature of NO follows a similar pattern to its rotational temperature, starting out right away at values well above the initial vibrational temperatures of the other two diatoms. This, again is consistent with what was observed for the isothermal case in Fig. 1(b). The internal temperatures of Fig. 6(c), representing the combined degree of rotational and vibrational excitation, exhibit behavior somewhere between those observed in Figs. 6(a) and (b), as would be expected. They are plotted here primarily because their time-averaged values over the indicated "pdf sampling period" will be of interest when examining the diatomic species' internal energy distributions in Fig. 8.

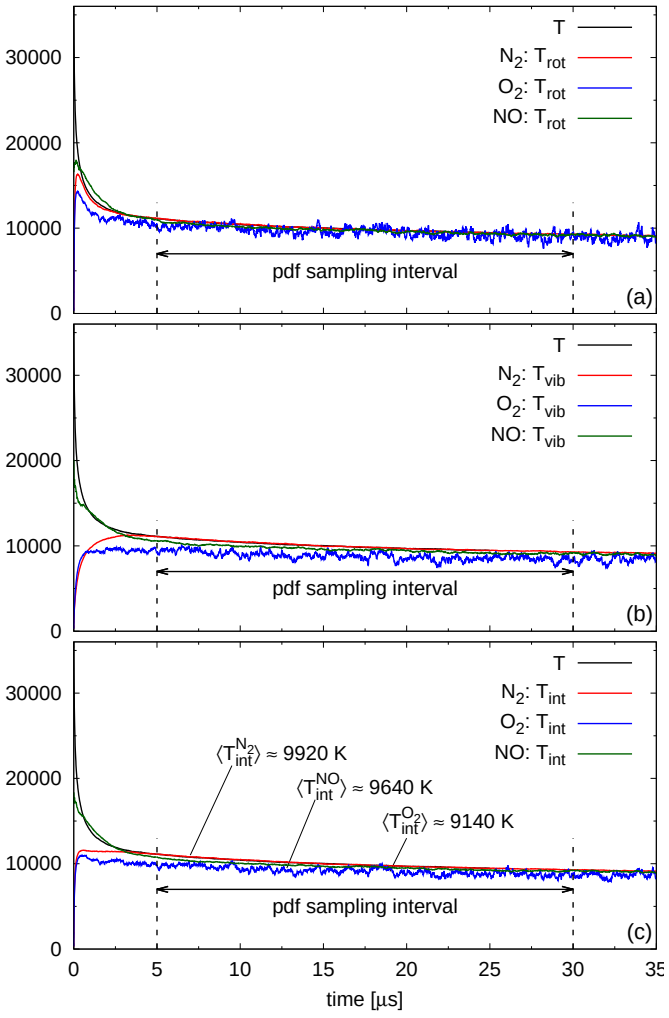

Fig 6. DMS of adiabatic reactor at $h_2 = 17.92\,\mathrm{MJ/kg}$: rotational (upper plot), vibrational (middle plot) and internal (bottom plot) temperature profiles [K] for N_2 (red), O_2 (blue) and NO (green)

Figure 7 shows the evolution of all five species' mole fractions in the adiabatic reactor over the same 35-μs time frame. The labeling conventions are the same as those used for the isothermal reactor plot from Fig. 2. When comparing both cases, there are common trends, but also some noticeable differences.

First, in both cases molecular oxygen (continuous blue line) disappears quickly from the mixture and only trace amounts of O_2 remain for the remainder of the simulated time. Simultaneously, nitric oxide is quickly being produced (continuous green line). After reaching its maximum of around 17%, the mole fraction of NO begins to decrease. This decline appears to be more gradual under adiabatic than under isothermal conditions. The biggest difference between the isothermal and adiabatic cases can be observed in the mole fraction profiles of molecular and atomic nitrogen. Looking back at the solid red line in Fig. 2, we see that the mole fraction of N_2 exhibits two distinct near-linear decrease phases. The first one lasts approximately from $t = 0$ to $0.75\,\mu$s. After a small induction time at the very beginning, the mole fraction of N_2 decreases rapidly from 80% to about 60% during this phase. Beyond this moment, the rate of decrease is noticeably slower, though it remains nearly linear for the remaining simulated time. At the same time, the mole fraction of atomic nitrogen (dashed red line in Fig. 2 increases in an almost linear fashion without interruption under isothermal conditions. By contrast, the N_2 mole fraction in the adiabatic reactor (solid red line in Fig. 7) exhibits a more uniform decrease. It starts out quickly without any delay and, within the first $2 - 3\,\mu$s drops from 80% to just below 60%. From there on, the N_2-profile transitions smoothly into a much slower rate of descent. The change in slope roughly coincides with the moment when the adiabatic reactor settles into its own slow cooling phase marked by a slowly decreasing translational temperature. Compared to the isothermal case, the mole fraction of atomic nitrogen rises more slowly in the adiabatic reactor. Toward the end of the first 35 simulated microseconds its increases only at a slow rate and has barely surpassed 20%.

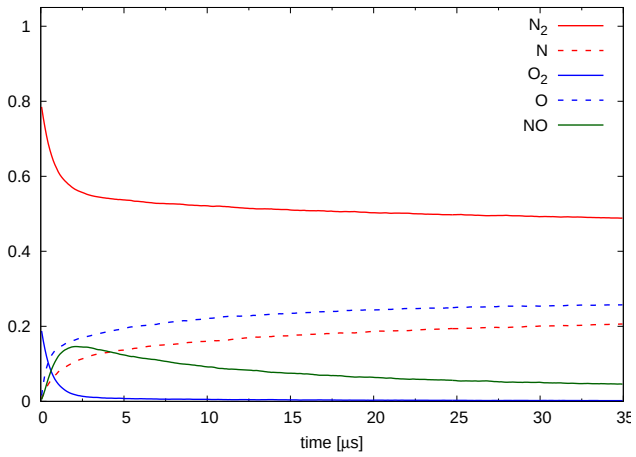

Fig 7. DMS of adiabatic reactor at $h_2 = 17.92\,$MJ/kg: mole fractions of air-5 species N_2 solid red, N dashed red, O_2 solid blue, O dashed blue, NO solid green line.

As was alluded to before, the gas in the adiabatic reactor undergoes two distinct phases. Early on, the large amount of energy stored in the translational mode is quickly used up to rovibrationally excite and partially dissociate the mixture. Once this phase is over, the translational and internal mode temperatures have almost leveled off to a common value. From there on, any changes in the gas thermodynamic state occur at a much slower rate. The system effectively settles into a slowly cooling QSS-like dissociation regime and the reservoir temperature decreases at a much slower pace. Judging from the temperature profiles of Fig. 6, the second phase begins approximately $5\,\mu$s into the simulation. Starting from this instant, a period lasting 25 microseconds has been labeled "pdf sampling phase". In a manner analogous to the "QSS phase" of Sec. 2.1, we use this time to gather time-averaged internal energy distributions of the three diatomic species, as well as reaction pdfs for the reactions listed in Table 1. The time-averaged internal (rotational + vibrational) energy population distributions for N_2 (red), O_2 (blue) and NO (green symbols) during this sampling phase are plotted in Figs. 8(a), (b) and (c) respectively. The time-averaged internal temperatures during the pdf sampling interval were listed in Fig. 6(c). By coincidence, these temperatures are almost identical with those during the QSS phase in the isothermal reactor from Sec. 2.1. Thus, the Boltzmann distributions shown using black symbols for

reference in Fig. 8 are effectively identical with those from Fig. 3. Just as under isothermal conditions, the internal energy distributions of all three diatomic species in the adiabatic reactor case are depleted at energies near and above their respective dissociation limits. Despite the statistical noise affecting the high-energy tail of the distributions in Figs. 8(a)-(c), the gap relative to the respective Boltzmann distributions is clearly visible.

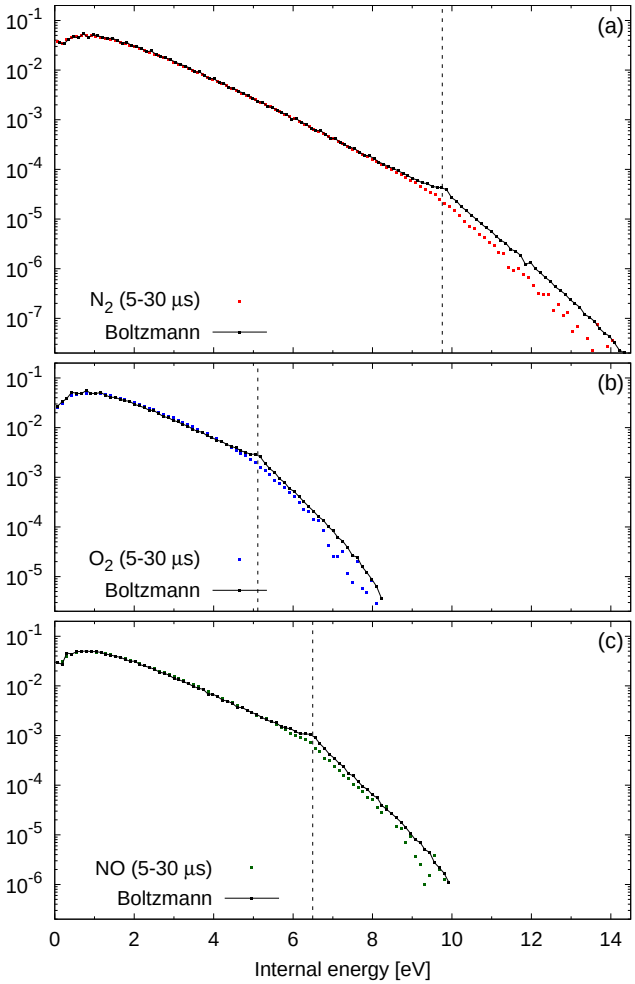

Fig 8. DMS of adiabatic reactor at $h_2 = 17.92\,\mathrm{MJ/kg}$: Normalized population distributions of diatomic species during $5-30\,\mu$s sampling phase. Boltzmann distributions for each diatom at $\langle T_{\mathrm{int}} \rangle$ during $5-30\,\mu$s sampling phase.

The time-averaged dissociation (red symbols) and exchange pdfs (blue symbols) for reactant pair N_2 + O from the adiabatic reactor are plotted in Fig. 9(a). Both curves exhibit similarities to the corresponding reaction pdfs from Fig. 4(a), gathered independently during the QSS phase in the isothermal reactor. Two main differences between the pdfs from the isothermal and adiabatic reactors should be emphasized. First, in the latter case the gas translational temperature is slowly changing over the sampling time, whereas it is maintained constant in the former. Thus, the reaction pdfs shown for the adiabatic case should be understood as blurred-out time-averaged versions of the slowly evolving instantaneous reaction pdfs over the duration of the sampling period. Second, the number of reaction events (both for dissociation and exchange) recorded in the $5-30\,\mu$s sampling window is significantly smaller than the number recorded over the $1-9\,\mu$s QSS phase for the isothermal reactor. This fact is responsible for the greater statistical noise apparent in the adiabatic case results. Aside from these differences though, in both cases the N_2 + O dissociation pdfs (red symbols in Figs. 9(a) and 4(a)) exhibit broadly similar

shapes, with characteristic peaks around molecular nitrogen's dissociation energy limit of 9.75 eV. The exchange pdfs (blue symbols in both plots) in both the isothermal and adiabatic cases also broadly follow the same shapes and a similar assessment can be made when comparing the reaction pdfs for reactant pair NO + N in Figs. 9(b) and 4(b) respectively.

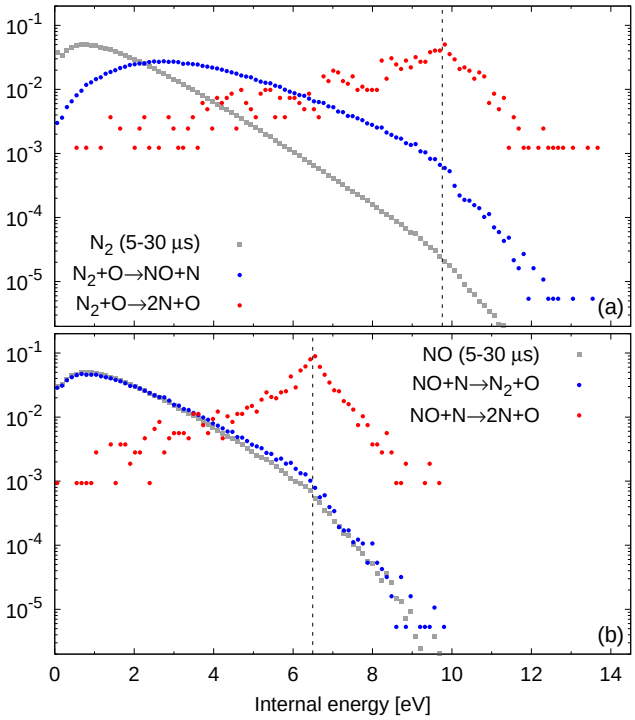

Fig 9. DMS of adiabatic reactor at $h_2 = 17.92$ MJ/kg: Normalized distributions for reactant pairs N_2 + O and NO + N during $5 - 30\,\mu$s sampling phase

Finally, the time-averaged dissociation (red symbols) and exchange (blue symbols) pdfs for reactant pairs O_2 + N and NO + O are plotted in Figs. 9(a) and (b) respectively. These results continue the pattern established by the preceding reactions in that the pdfs gathered in the adiabatic reactor closely resemble those from Figs. 5(a) and (b), which were previously gathered during QSS phase under isothermal conditions.

3. Conclusions

In this work we have presented first-principles direct molecular simulations of internal energy relaxation, coupled with nonequilibrium dissociation and exchange reactions in a five-species air mixture. Expanding upon previous work, the calculations reported here were carried out both under isothermal and adiabatic conditions. We gathered internal energy population distributions of the three diatomic species (N_2, O_2 and NO) during the quasi-steady-state dissociation regime following the initial rotational-vibrational energy excitation phases. All three species, both under isothermal and adiabatic conditions consistently exhibited depleted high-energy tails relative to their respective Boltzmann distributions. Furthermore, we gathered reaction probability density functions for dissociation and exchange of reactant pairs N_2 + O, NO + N, O_2 + N and NO + O during the QSS phase. For all four reactant pairs, the dissociation pdfs exhibit strong selectivity toward molecules with internal energies near the diatomic species' respective dissociation limit. Highly preferential dissociation from energy levels near D_0 and above was observed consistently for all diatomic species during the QSS phase, despite the aforementioned depletion of the population distributions' high-energy tails. Such findings are consistent with prior DMS studies of nonequilibrium dissociation involving separate N_2 – N and O_2 – O mixtures. By contrast, the exchange

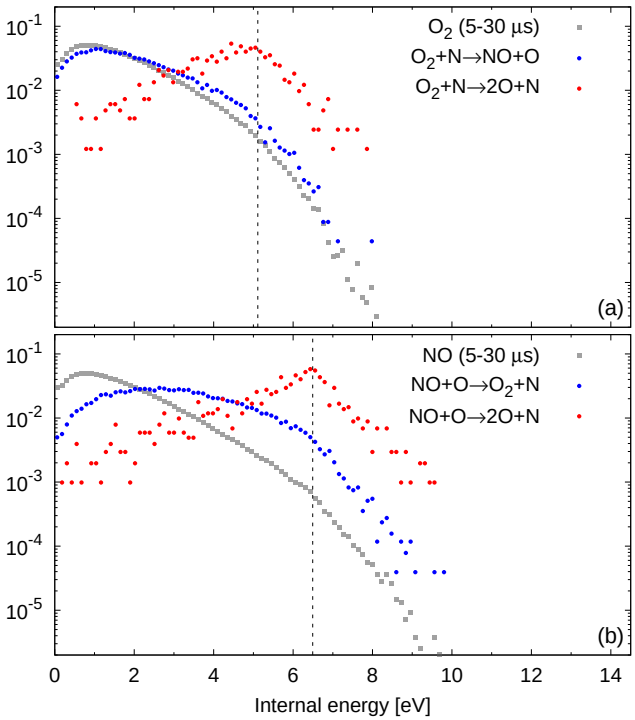

Fig 10. DMS of adiabatic reactor at $h_2 = 17.92$ MJ/kg: Normalized distributions for reactant pairs O_2 + N and NO + O during $5 - 30\,\mu$s sampling phase

pdfs do not exhibit the same bias toward specific internal energy ranges.

We are currently in the process of extending the DMS studies presented here to a wider range of conditions, both in terms of isothermal reservoir temperatures and adiabatic reactor enthalpies. This will allow us to generate a suite of benchmark solutions for calibrating newly developed chemical kinetic models for use in Computational Fluid Dynamics codes. In future work, we plan to also study normal shocks of 5-species air directly with DMS and compare these calculations against concurrent CFD solutions.

Acknowledgments

This work was carried out with support from AFOSR grant FA9550-19-1-0219 and NASA grant 80NSSC20K1061

References

[1] G.A. Bird. *Molecular Gas Dynamics and the Direct Simulation of Gas Flows*. Oxford University Press, 1994.

[2] R.L. Jaffe, D.W. Schwenke, and M. Panesi. *First principles calculation of heavy particle rate coefficients*, volume 247, chapter 3, pages 103–158. American Institute of Aeronautics and Astronautics, 2015.

[3] J.D. Bender, P. Valentini, I. Nompelis, Y. Paukku, Z. Varga, D.G. Truhlar, T.E. Schwartzentruber, and G.V. Candler. An improved potential energy surface and multi-temperature quasiclassical trajectory calculations of $N_2 + N_2$ dissociation reactions. *The Journal of Chemical Physics*, 143:054304, 2015.

[4] K. Koura. Monte Carlo direct simulation of rotational relaxation of diatomic molecules using classical trajectory calculations: Nitrogen shock wave. *Physics of Fluids*, 9:3543, 1997.

[5] K. Koura. Monte Carlo direct simulation of rotational relaxation of nitrogen through high total temperature shock waves using classical trajectory calculations. *Physics of Fluids*, 10:2689, 1998.

[6] P. Norman, P. Valentini, and T.E. Schwartzentruber. GPU-Accelerated Classical Trajectory Calculation Direct Simulation Monte Carlo Applied to Shock Waves. *Journal of Computational Physics*, 247:153–167, 2013.

[7] T.E. Schwartzentruber, M.S. Grover, and P. Valentini. Direct Molecular Simulation of Nonequilibrium Dilute Gases. *Journal of Thermophysics and Heat Transfer*, 32(4):892–903, 2018.

[8] P. Valentini, T.E. Schwartzentruber, J.D. Bender, I. Nompelis, and G.V. Candler. Direct molecular simulation of nitrogen dissociation based on an ab initio potential energy surface. *Physics of Fluids*, 27:086102, 2015.

[9] P. Valentini, T.E. Schwartzentruber, J.D. Bender, and G.V. Candler. Dynamics of nitrogen dissociation from direct molecular simulation. *Physical Review Fluids*, 1:043402, 2016.

[10] Y. Paukku, K.R. Yang, Z. Varga, and D.G. Truhlar. Global ab initio ground-state potential energy surface of N_4. *The Journal of Chemical Physics*, 139:044309, 2013.

[11] M.S. Grover, E. Torres, and T.E. Schwartzentruber. Direct molecular simulation of internal energy relaxation and dissociation in oxygen. *Physics of Fluids*, 31:076107, 2019.

[12] M.S. Grover, T.E. Schwartzentruber, Z. Varga, and D.G. Truhlar. Vibrational energy transfer and collision-induced dissociation in $O + O_2$ collisions. *Journal of Thermophysics and Heat Transfer*, 33(3):797–807, 2019.

[13] Y. Paukku, K.R. Yang, Z. Varga, G. Song, J.D. Bender, and D.G. Truhlar. Potential energy surfaces of quintet and singlet O_4. *The Journal of Chemical Physics*, 147:034301, 2017.

[14] Y. Paukku, Z. Varga, and D.G. Truhlar. Potential energy surface of triplet O_4. *The Journal of Chemical Physics*, 148:124314, 2018.

[15] Z. Varga, Y. Paukku, and D.G. Truhlar. Potential energy surfaces for $O + O_2$ collisions. *The Journal of Chemical Physics*, 147:154312, 2017.

[16] E. Torres and T.E. Schwartzentruber. Direct molecular simulation of nitrogen dissociation under adiabatic post-shock conditions. *Journal of Thermophysics and Heat transfer*, 34(4):801–815, 2020.

[17] E. Torres and T.E. Schwartzentruber. Direct molecular simulation of dissociating oxygen under adiabatic and normal shock wave conditions. In *AIAA Scitech 2021 Forum*, 2021. AIAA 2021-0318.

[18] E. Torres and T.E. Schwartzentruber. Direct molecular simulation of oxygen dissociation across normal shocks. *Theoretical and Computational Fluid Dynamics*, 36(1):41–80, 2022.

[19] P. Valentini, M.S. Grover, N. Bisek, and A. Verhoff. Molecular simulation of flows in thermochemical non-equilibrium around a cylinder using ab initio potential energy surfaces for $N_2 + N$ and $N_2 + N_2$ interactions. *Physics of Fluids*, 33(9):096108, 2021.

[20] M.S. Grover and P. Valentini. Ab initio simulation of hypersonic flows past a cylinder based on accurate potential energy surfaces. *Physics of Fluids*, 33(5):051704, 2021.

[21] Z. Varga, R. Meana-Pañeda, G. Song, Y. Paukku, and DG Truhlar. Potential energy surface of triplet N_2O_2. *The Journal of chemical physics*, 144(2):024310, 2016.

[22] W. Lin, Z. Varga, G. Song, Y. Paukku, and D.G. Truhlar. Global triplet potential energy surfaces for the $N_2(X^1\Sigma)+O(^3P) \rightarrow NO(X^2\Pi)+N(^4S)$ reaction. *The Journal of Chemical Physics*, 144:024309, 2016.

[23] E. Torres, E.C. Geistfeld, and T.E. Schwartzentruber. Direct molecular simulation of rovibrational relaxation and chemical reactions in air mixtures. In *AIAA SCITECH 2022 Forum*, 2022.

[24] E. Torres, T. Gross, E. Geistfeld, and T.E. Schwartzentruber. Verification of nonequilibrium thermochemistry models for hypersonic cfd by first-principles simulation. In *Eleventh International Conference on Computational Fluid Dynamics (ICCFD11)*, 2022. ICCFD11-2022-2201.

[25] R.L. Macdonald, E. Torres, T.E. Schwartzentruber, and M. Panesi. State-to-state master equation and direct molecular simulation study of energy transfer and dissociation for the $N_2 - N$ system. *The Journal of Physical Chemistry A*, 2020.

[26] R.L. Macdonald, M.S. Grover, T.E. Schwartzentruber, and M. Panesi. Construction of a coarse-grain quasi-classical trajectory method. II. Comparison against the direct molecular simulation method. *The Journal of Chemical Physics*, 148(5):054310, 2018.